Construction of the optical part of a time-of-flight detector prototype for the AFP detector

L. Nozka,[1,*] **L. Adamczyk,**[2] **G. Avoni,**[3] **A. Brandt,**[4] **P. Buglewicz,**[5] **E. Cavallaro,**[6] **G. Chiodini,**[7] **L. Chytka,**[1] **K. Ciesla,**[5] **P.M. Davis,**[8] **M. Dyndal,**[2] **S. Grinstein,**[6] **P. Hamal,**[1] **M. Hrabovsky,**[1] **K. Janas,**[2] **K. Jirakova,**[1] **M. Kocian,**[9] **T. Komarek,**[1] **K. Korcyl,**[5] **J. Lange,**[6] **D. Mandat,**[1] **V. Michalek,**[1] **I. Lopez Paz,**[6] **D. Northacker,**[10] **M. Rijssenbeek,**[10] **L. Seabra,**[11] **P. Schovanek,**[1] **R. Staszewski,**[5] **P. Swierska,**[5] **and T. Sykora**[12]

[1]*Palacky University, RCPTM, Olomouc, Czech Republic*
[2]*AGH University of Science and Technology, Faculty of Physics and Applied Computer Science, al. Mickiewicza 30, PL-30059 Cracow, Poland*
[3]*INFN Bologna and Universita di Bologna, Dipartimento di Fisica, viale C. Berti Pichat, 6/2, IT – 40127 Bologna, Italy*
[4]*The University of Texas at Arlington, Department of Physics, Box 19059, Arlington, TX 76019, USA*
[5]*H. Niewodniczanski Institute of Nuclear Physics PAN, Cracow, Poland*
[6]*Institut de Fisica d'Altes Energies, Universitat Autonoma de Barcelona, Edifici Cn, ES - 08193 Bellaterra (Barcelona), Spain*
[7]*INFN Lecce and Universita del Salento, Dipartimento di Fisica, Via Arnesano IT - 73100 Lecce, Italy*
[8]*Centre for Particle Physics, Department of Physics, University of Alberta, Edmonton, AB T6G 2G7, Canada*
[9]*Stanford Linear Accelerator Center, Stanford, California 94309, USA*
[10]*Stony Brook University, Dept. of Physics and Astronomy, Nicolls Road, Stony Brook, NY 11794-3800, USA*
[11]*Laboratorio de Instrumentacao e Fisica Experimental de Particulas, LIP, Av. Elias Garcia 14, Lisbon, Portugal*
[12]*Charles University in Prague, Faculty of Mathematics and Physics, Institute of Particle and Nuclear Physics, V Holesovickach 2, CZ - 18000 Praha 8, Czech Republic*
*libor.nozka@upol.cz

Abstract: We present the construction of the optical part of the ToF (time-of-flight) subdetector prototype for the AFP (ATLAS Forward Proton) detector. The ToF detector in conjunction with a 3D silicon pixel tracker will tag and measure protons originating in central exclusive interactions p + p → p + X + p, where the two outgoing protons are scattered in the very forward directions. The ToF is required to reduce so-called pileup backgrounds that arise from multiple proton interactions in the same bunch crossing at high luminosity. The background can fake the signal of interest, and the extra rejection from the ToF allows the proton tagger to operate at the high luminosity required for measurement of the processes. The prototype detector uses fused silica bars emitting Cherenkov radiation as a relativistic particle passes through it. The emitted Cherenkov photons are detected by a micro-channel plate multi-anode Photomultiplier Tube (MCP-PMT) and processed by fast electronics.

References and links

1. M. G. Albrow and A. Rostovtsev, "Searching for the Higgs boson at hadron colliders using the missing mass method," https://arxiv.org/abs/hep-ph/0009336 (2000).
2. A. B. Kaidalov, V. A. Khoze, A. D. Martin, and M. G. Ryskin, "Extending the study of the Higgs sector at the LHC by proton tagging," Eur. Phys. J. C **33**(2), 261–271 (2004).
3. J. Bonnet, J. Liao, and K. Piotrzkowski, "Study on GASTOF – A 10 ps resolution timing detector," Nucl. Instrum. Methods Phys. Res. A **762**, 77–84 (2014).

4. L. Nozka, A. Brandt, M. Rijssenbeek, T. Sykora, T. Hoffman, J. Griffiths, J. Steffens, P. Hamal, L. Chytka, and M. Hrabovsky, "Design of Cherenkov bars for the optical part of the time-of-flight detector in Geant4," Opt. Express **22**(23), 28984–28996 (2014).
5. M. G. Albrow, H. Kim, S. Los, M. Mazzillo, E. Ramberg, A. Ronzhin, V. Samoylenko, H. Wenzel, and A. Zatserklyaniy, "Quartz Cherenkov counters for fast timing: QUARTIC," J. Instrum. **7**(10), P10027 (2012).
6. ATLAS-TDR-024–2015, 2015.
7. J. Lange, E. Cavallaro, S. Grinstein, and I. L. Paz, "3D silicon pixel detectors for the ATLAS Forward Physics experiment," J. Instrum. **10**(03), C03031 (2015).
8. PHOTONIS USA Pennsylvania, Inc., XPM85112 datasheet.
9. Epoxy Technology, Inc., Epotek 305 datasheet.
10. S. Agostinelli, J. Allison, K. Amako, J. Apostolakis, H. Araujo, P. Arce, M. Asai, D. Axen, S. Banerjee, G. Barrand, F. Behner, L. Bellagamba, J. Boudreau, L. Broglia, A. Brunengo, H. Burkhardt, S. Chauvie, J. Chuma, R. Chytracek, G. Cooperman, G. Cosmo, P. Degtyarenko, A. Dell'Acqua, G. Depaola, D. Dietrich, R. Enami, A. Feliciello, C. Ferguson, H. Fesefeldt, G. Folger, F. Foppiano, A. Forti, S. Garelli, S. Giani, R. Giannitrapani, D. Gibin, J. J. Gómez Cadenas, I. González, G. Gracia Abril, G. Greeniaus, W. Greiner, V. Grichine, A. Grossheim, S. Guatelli, P. Gumplinger, R. Hamatsu, K. Hashimoto, H. Hasui, A. Heikkinen, A. Howard, V. Ivanchenko, A. Johnson, F. W. Jones, J. Kallenbach, N. Kanaya, M. Kawabata, Y. Kawabata, M. Kawaguti, S. Kelner, P. Kent, A. Kimura, T. Kodama, R. Kokoulin, M. Kossov, H. Kurashige, E. Lamanna, T. Lampén, V. Lara, V. Lefebure, F. Lei, M. Liendl, W. Lockman, F. Longo, S. Magni, M. Maire, E. Medernach, K. Minamimoto, P. Mora de Freitas, Y. Morita, K. Murakami, M. Nagamatu, R. Nartallo, P. Nieminen, T. Nishimura, K. Ohtsubo, M. Okamura, S. O'Neale, Y. Oohata, K. Paech, J. Perl, A. Pfeiffer, M. G. Pia, F. Ranjard, A. Rybin, S. Sadilov, E. Di Salvo, G. Santin, T. Sasaki, N. Savvas, Y. Sawada, S. Scherer, S. Sei, V. Sirotenko, D. Smith, N. Starkov, H. Stoecker, J. Sulkimo, M. Takahata, S. Tanaka, E. Tcherniaev, E. Safai Tehrani, M. Tropeano, P. Truscott, H. Uno, L. Urban, P. Urban, M. Verderi, A. Walkden, W. Wander, H. Weber, J. P. Wellisch, T. Wenaus, D. C. Williams, D. Wright, T. Yamada, H. Yoshida, and D. Zschiesche, "Geant4—a simulation toolkit," Nucl. Instrum. Methods Phys. Res. A **506**(3), 250–303 (2003).
11. McPherson,Inc., VUVAS 2000 datasheet.
12. P. M. Duarte, "QUARTIC: An ultra-fast time-Of-flight counter," M.Sci. Thesis, The University of Texas, Arlington, 2007.
13. J. Lange, L. Adamczyk, G. Avoni, E. Banas, A. Brandt, M. Bruschi, P. Buglewicz, E. Cavallaro, D. Caforio, G. Chiodini, L. Chytka, K. Ciesla, P. M. Davis, M. Dyndal, S. Grinstein, K. Janas, K. Jirakova, M. Kocian, K. Korcyl, I. L. Paz, D. Northacker, L. Nozka, M. Rijssenbeek, L. Seabra, R. Staszewski, P. Swierska, and T. Sykora, "Beam Tests of an Integrated Prototype of the ATLAS Forward Proton Detector," J. Instrum. **11**(09), P09005 (2016).

1. Introduction

Precision timing is useful for many applications, ranging from Positron Electron Tomography (PET) scans to particle physics. For PET scans, information about the time difference of the arriving photons helps improve the position resolution by determining the location of the electron-positron pair annihilation, while for high energy physics, it has typically been used in conjunction with a momentum measurement to determine the mass of the particle, which in turn defines the particle's identity. Timing detectors can be used as well as a part of the proton tagging detectors to decrease the background to central exclusive production (CEP) events $p + p \rightarrow p + X + p$ where X stands for the centrally produced system, which could consist of a pair of jets or particles, a pair of intermediate vector bosons (W^+W^-), or even a Higgs boson H [1, 2].

At high luminosity, the environment of the Large Hadron Collider (LHC) places stringent demands on the timing detectors: high resolution (~10 – 20 ps, equivalent to 2.1 – 4.2 mm interaction vertex resolution), high rate capability (5 to 10 MHz), radiation hardness (integrated charge of 10 C/cm2/yr), and multi-proton detection capabilities. ToF detectors based on Cherenkov emission in fused silica radiators are treated as an optimal choice. On the other hand, detectors based on emission in a gas, for instance the GASTOF detector with C_4F_{10} gas [3], have better intrinsic time resolution but a low signal level. Back to fused silica, relativistic protons emit a Cherenkov light pulse in the UV region (in the 200 to 400 nm range predominantly) in a Cherenkov cone of 48 degrees. The radiator also acts as a light guide to direct the light to a sensor with a high quantum efficiency in the UV region. Typically a fast micro-channel plate multi-anode Photomultiplier Tube (MCP-PMT) or a silicon photomultiplier (SiPM) is used. A multi-channel MCP-PMT is an option where pixelization is required. Which is also the case of the detector in this study.

The ToF design described here is based on benchmark studies published in [4]. These studies introduced several key concepts adopted in the final design and construction of the ToF prototype. The main design feature is an L-shape geometry, Fig. 1(a), first introduced by M. Albrow and his group [5]. Here we denote a bar arm crossing the beam as the radiator whilst an arm leading towards the sensor as the light guide. Albrow's design is based on the light propagation by virtue of total reflections on the bar sides. On the other hand, our design largely relies on a direct fast light propagation to the sensor (approximately 60% of all photon tracks in a bar accepted by the sensor). This means a bar has to be rotated so that its radiator is tilted by the Cherenkov angle of 48 degrees with respect to the beam axis, see Fig. 1(a). In addition, direct pathways need to be reflected on the bar elbow which means a 45 degrees cut coated with an appropriate reflection layer. The part of the light propagated using total reflections is delayed with respect to the fast direct propagation. The aforementioned studies proposed a so-called taper to speed-up total-reflection pathways. On the other hand, adding a taper results in a correspondingly thinner radiator of a lower acceptance, see Fig. 1(a). Moreover, a radiator cut is another design improvement allowing higher signal due to the additional back reflection light with details described in [4].
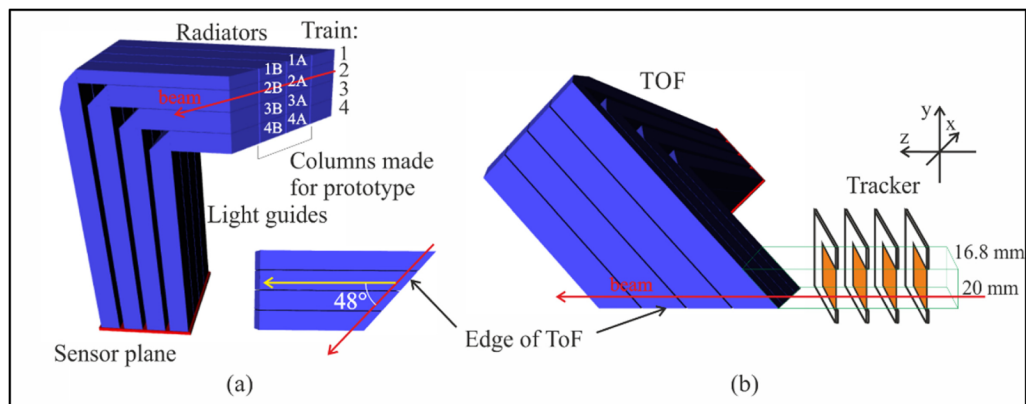

Fig. 1. (a) Geometry of the ToF, (b) the ToF with the tracker modules (not in scale).

2. Design of the ToF detector prototype

The AFP detector [6] is composed of four stations, two stations on each side of the ATLAS Interaction Point at distances of 206 m (inner stations) and 214 m (outer stations). Inner stations consist of silicon detectors (trackers) [7] placed in dedicated Roman pots while outer stations consist of trackers accompanied by time-of-flight detectors (in identical Roman pots as well), see Fig. 1(b). In the figure, the coordinate system is chosen so that the beam axis is parallel to the z axis, the x axis is horizontal and the y axis is vertical. The aim of the tracker is to precisely measure the trajectory of scattered protons while the aim of the ToF detector is to reject the so-called pileup background which can fake the signal of interest.

The ToF part has to fulfill the following performance requirements: time resolution below 20 ps, radiation hardness up to 700 kGy (3×10^{15} n_{eq} cm^{-2}, at a distance of 5 mm from the beam axis) [6], high rate capability (5 to 10 MHz), and multi-proton detection capabilities (~1 background proton/detector is expected per bunch crossing at standard luminosity).

The AFP detector acceptance is 16.8×20.0 mm^2 given by the tracker dimensions [7] as illustrated in Fig. 1(b). From the ToF point of view the area is divided into four segments alongside the x axis. Each segment is composed of a set of four bars denoted as a train, see Fig. 1(a). This arrangement results in a matrix of 4×4 bars. This division is closely related to Photonis XPM85112 MCP-PMT (miniPlanacon) with 4×4 channel pixelization [8]. This detector was chosen for its enhanced timing performance (transit-time spread, TTS, below 35 ps at 405 nm) and its dimensions.

Dimension constraints to the ToF are due to the limited space inside the Roman pot and due to the pixel size 6.25×6.25 mm^2 of the PMT. The first factor predetermines the overall L-shape of bars (and the optical part of ToF as a whole) while the pixel size determines the cross-section dimensions of the bars. Bars of each train have light guide arms of the same dimensions. On the other hand, each radiator is unique in its dimensions. Their length is set so that their cut sides lie in one plane called the edge of the ToF (bottom-cut plane), see Fig. 1.

For the first prototype, we did not construct the whole matrix of 4×4 bars. Instead, we decided to produce a matrix 2×4 of bars so that the middle columns were produced, see also Fig. 1(a). Such a configuration was sufficient for integration tests (tracker and ToF integration) and initial performance studies. Bars were labelled as indicated in Figs. 1(a) and 2(b): 1A and 1B in the train 1 etc. with the A bars in the front as seen from the beam direction.

3. Construction of the bars

The bars of the AFP ToF detector are L-shaped and made of suprasil. There is a possibility to produce L-shaped bars as one piece [5]. In our design there are at least two cuts (45 or 48 degrees) plus optionally the taper cut (18 degrees). It was difficult to construct such bars as one suprasil piece assumed dimension tolerances and polishing precision (see below). Instead we decided to produce the light guide and the radiator separately and glue them together, see Fig. 2(a).
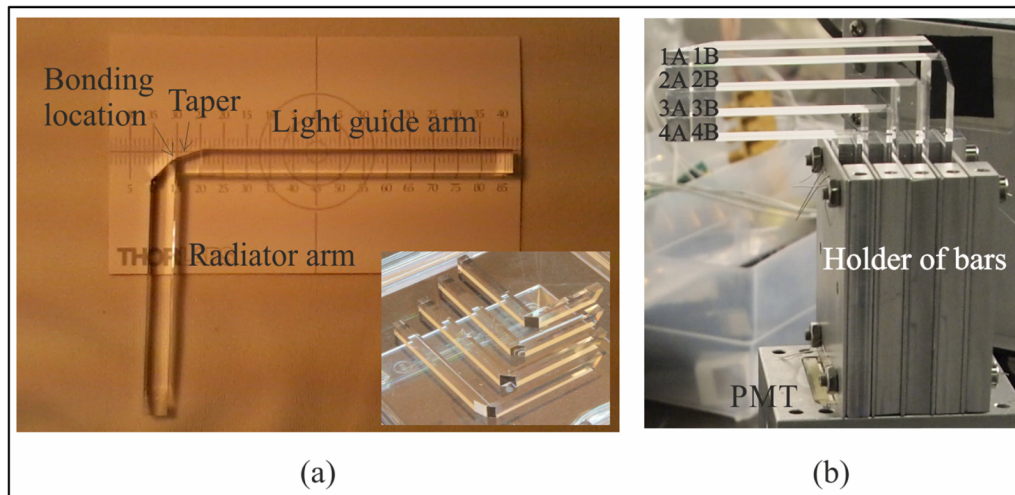

Fig. 2. (a) Example of a fused silica bar with the taper and a set of bars, (b) the set of 2x4 bars forming the ToF prototype.

The dimensions of the bars for the ToF prototype are summarized in the Table 1. The dimension tolerances are: ± 0.05 mm for all dimensions of the light guide and cross-section dimensions of the radiator, ± 0.1 mm for the length of the radiator, and ± 2' (± 0.017 degrees) for cuts. The higher tolerance for the length of the radiator is due to the two cuts resulting in two sharp edges preventing stringent toleration. Polishing precision was stated to three interference fringes at 550 nm. It was decided to coat the elbow cut with a reflection layer made of aluminum with a thickness of at least 200 nm and protected by a SiO$_2$ layer of the thickness 120 nm (protection against oxidation and mechanical abrasion). The deposition was carried out by means of a standard PVD (Physical Vacuum Deposition) technique.

Table 1. Dimensions of the bars for the ToF prototype in millimeters.

Train	A bars		B bars	
	Radiator	Light guide	Radiator	Light guide
1	3 × 6 × 57.8	5 × 6 × 70.3	3 × 6 × 52.2	5 × 6 × 70.3
2	5 × 6 × 53.5	5 × 6 × 65.2	5 × 6 × 47.9	5 × 6 × 65.2
3	5 × 6 × 47.3	5 × 6 × 60.1	5 × 6 × 41.7	5 × 6 × 60.1
4	5 × 6 × 41.0	5 × 6 × 55.0	5 × 6 × 35.4	5 × 6 × 55.0

All pieces (the radiators and the light bars) were produced from a bulk of suprasil material. We used approximately 150 g of a suprasil bulk to produce all pieces as listed in Table 1 (the total weight 53 g) and spares for miscellaneous testing. Cutting, milling, and polishing were carried out by means of a common optical technology. By design, the light guides were produced in the form of pure cuboids. Since the light guides have the same length in a given train, they were made at once. As each radiator has a unique length their uncut intermediates were produced piece by piece. There are two cuts at each end side of the radiator (45 and 48 degrees rotated by 90 degrees with respect to each other). For a given cut type, radiators were cut together (per four pieces).

Finally, radiators and light guides were glued together. Nowadays UV cementation is the most popular technique for bonding optical surfaces allowing fast, precise, and handy manipulation. However, this technique is only applicable for optical solutions in visible and infrared region because UV cements significantly absorb UV light. Finally we decided to use the Epotek 305 epoxy glue [9] assuring high transparency down to 250 nm and sufficient transparency down to 235 nm. The thickness of the glue layer did not exceed 20 μm which is the standard tolerance in the optics designing.

4. Constraints given by the materials

Construction of the bar includes the mirror production and optical coupling of the radiator and the light guide by means of an optical cement. These extra factors generally introduce other signal losses due to the transmittance of glue and mirror reflection. Here we report the results of the analysis of signal attenuation due to both factors. In addition, signal attenuation of suprasil itself is reported.

4.1 Mirror performance

Reflectivity of an optical surface is, in general, a function of the polarization state of the incident light. Cherenkov light is linearly polarized with polarization vector perpendicular to the Cherenkov cone. The calculated reflectance profile of the bar mirror is drawn in Fig. 3(a) for the incidence angle of 45 degrees (valid for the prominent direct photon pathways). The distributions of s and p polarization components on the mirror were calculated by means of a Geant4 simulation [10]. Results are plotted in Fig. 3(b) in terms of their ratio s/p (normalized, logarithmic plot). The higher statistics is below $s/p<1$ (53% of the total amount) which means that the p component prevails (the peak is at 0.34). Back to Fig. 3(a), the reflectivity of the mirror elbow is between the red and the black curve (below 90%). This means a loss of 10 – 12% in the wavelength region from 200 nm to 400 nm which is of the most interest (see Introduction above and [4]). One can obtain a higher reflectivity by means of a dielectric mirror made of a system of a thin layer dielectric stack. For example, a system of 50 layers (better 70 layers) of SiO_2/HfO_2 will increase reflectivity by up to 96% in the wavelength region from 200 nm to 400 nm meaning a loss of 4% by reflection. However, we decided to use a simpler solution with aluminum coating for the ToF prototype assuming less light by 6% with respect to the dielectric solution.
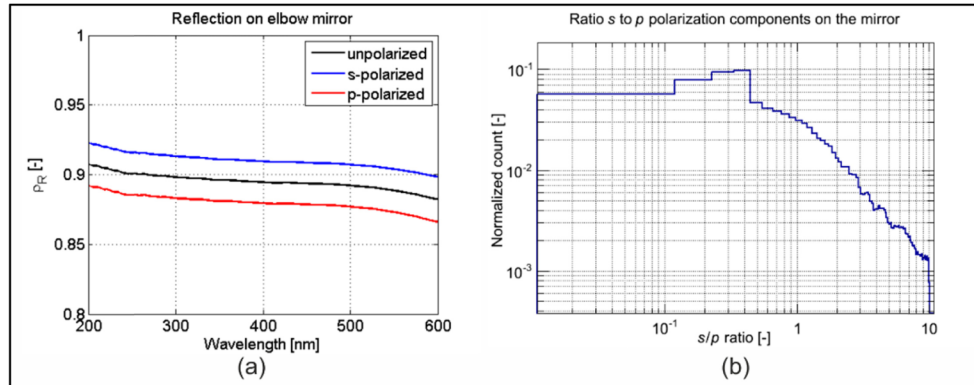
Fig. 3. (a) Reflectivity of the coated elbow cut, (b) ratio between the polarization components.

4.2 Transmittance of glue and suprasil

Figure 4(a) shows the results of transmittance measurements of suprasil and Epotek 305 glue. The measurements were performed with a DUV/UV spectrometer VUVAS 2000 ([11]). For the measurement of the suprasil itself, we used samples in the form of round suprasil pieces (20 mm diameter, 4 mm thick). Concerning transmittance measurements of the glue, we used samples in the form of two round suprasil pieces (20 mm diameter, 2 mm thick) bonded together with the glue. The red curve in the plot stands for the transmittance of the suprasil itself (including Fresnel reflection losses). Suprasil material of the thickness 4 mm cuts wavelengths below 166 nm (drop to half of the maximum). The blue curve corresponds to the transmittance of the whole system suprasil plus glue. Our results find a transparency edge at 233 nm. The transmission cut incorporates additional signal loss in the region below 233 nm.

Based on our simulations, the wavelengths accepted by the MCP-PMT are plotted in Fig. 4(b) with a significant loss region below 233 nm. A comparison was made for a bar without taper. Similar results stand for bars with taper. The calculated loss is about 18% – 19% (with or without a taper). This loss is valid for the wavelength region from 200 nm to 600 nm where the quantum efficiency of the photomultiplier is known [4, 12]. Thus the glue plays a significant role in attenuation of the signal.
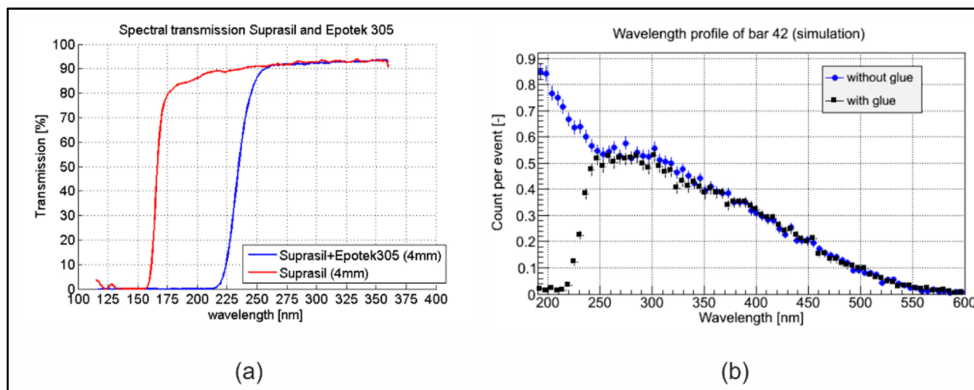

Fig. 4. (a) Measured transmittances of suprasil and Epotek 305, (b) spectral attenuation of Epotek 305 based on the accepted wavelength profile in the sensor (simulation, bar 1A).

5. Signal response of the bars

The ToF prototype was tested during two test campaigns at the CERN-SPS test-beam facility (120 GeV π + particles) in November 2014 and September 2015 in the frame of the AFP

integration test beam measurements [13]. The scheme of the measurement setup is shown in Fig. 5. The beam passed through the bars and the trigger. The trigger consisted of a 30 mm long fused silica bar of 3×3 mm^2 cross-section clamped to a silicon photomultiplier (SiPM). Its detection is also based on Cherenkov radiation. For the ToF module, each bar in the 2×4 matrix was brought into contact (without the use of optical grease) with the Planacon MCP-PMT XPM815112. It operated at the high voltage of 1870 V and the gain $5 \cdot 10^5$ for an optimal separation of the useful signal from the pedestal (rejection threshold at −100 mV, see below). The signal output the MCP-PMT was amplified by means of two-stage preamplifiers. Its first stage consisted of a current-to-voltage (A-V) converter with a 1 kΩ resistor and a voltage amplifier with the gain of 10. The second stage was a voltage amplifier with the same gain of 10. For raw signal studies, the amplified signal was then analyzed with a LeCroy SDA760ZI oscilloscope (6 GHz, 20 GS/s, 4 channels). For timing studies, the raw signal was preprocessed with a constant fraction discriminator (CFD). The CFD threshold level was set to −100 mV for the pedestal rejection. In both cases, the signal was triggered with the SiPM detector signal processed with another CFD module (here the threshold was set to −200 mV). The trigger detector was moved vertically in order to select a specific train for measurements.
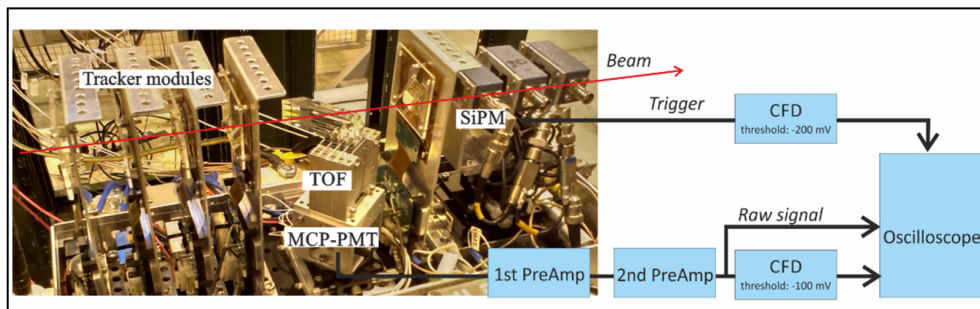

Fig. 5. Setup of the test beam measurements.

The following results are based on measurements with bars optically isolated from each other to prevent a possible undesired optical cross-talk between bars. Moreover they occupied separated pixels to prevent electronic cross-talk. The data was collected near the edge of the bars (area 3×3 mm^2 given by the SiPM trigger detector). The distributions of signal amplitudes of all bars are plotted in Fig. 6(a) in the form of boxplots. Each distribution is described by a blue box defining the interval from 25% (Q1) to 75% (Q2) quantiles of the distribution with a red level mark inside indicating the mean value M (50% quantile). The dash line with ending defines the interval from the minimum value to the maximum value of the distribution excluding outliers (red points). The lower outliers are the values lower than Q1-1.5*(Q2-Q1). The mean amplitude differs from bar to bar which is a result of their different geometry and different response among pixels of the PMT. Our laboratory tests with a femtosecond laser at 420 nm showed the mean amplitude variation of 7% among the pixels.

Despite their highest length, the bars in the first train (1A and 1B) generated the highest output (level of −350 mV in amplitude) by virtue of their taper modification. Other bars produced lower signal output with amplitudes around −250 mV on average (drop by 30%). These results confirm that the taper modification in the bar elbow increases the signal output of the bar as predicted by simulation studies [4].
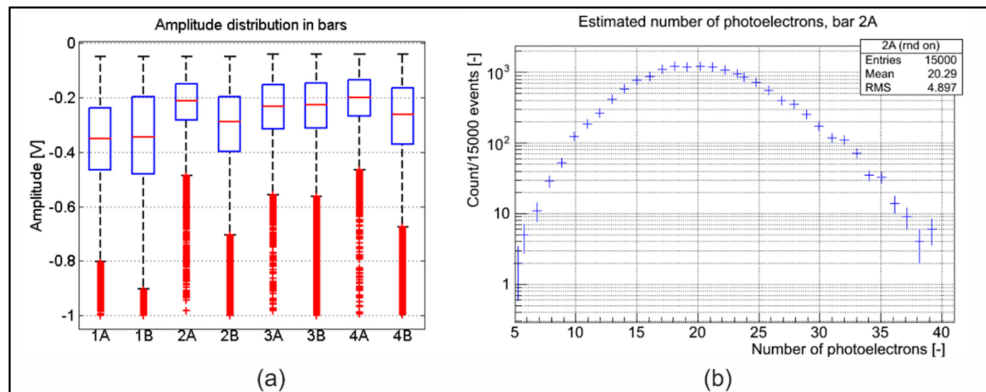
Fig. 6. (a) Distribution of the amplitude, (b) estimated distribution of generated photoelectrons given by simulation.

The signal outputs from all bars embody relatively high fluctuation (Q2-Q1)/M in the range of 30% – 40% given by the response of the PMT channels and by fluctuations of signal pathways in the bars. Fluctuations of the signal are the consequence of random processes existing in each stage of the signal chain starting with the Cherenkov emission and ending with the signal registration. The estimated fluctuation of the signal originating from the photomultiplier is about 7%, the same for all pixels (given by laser tests at 420 nm). Thus fluctuations of the signal in the optical part dominate. To understand the origin of such fluctuations we estimated the number of generated photoelectrons in our simulations (see [4] for details) and assumed the photodetection efficiency (PDE) of the PMT specified in [12].

In Fig. 6(b) the estimated number of photoelectrons (pe) produced per event is plotted for the model of bar 2A. It was calculated for randomly generated particle positions in a square of 3×3 mm^2 to mimic the SiPM trigger detector defining the area of acceptance. In terms of quantiles Q1 and Q2 defined above, Q1 = 17 pe and Q2 = 23 pe with the mean M = 20 pe (Fig. 6(b)) giving a fluctuation estimate of (Q2-Q1)/M = 30% which corresponds to the observed fluctuation level in the signal.

The 30% level fluctuations embody the variance of the number of generated Cherenkov photons, fluctuations in the bar (transport in the bar, reflections, escaping, attenuation of the glue), and fluctuations due to the PMT. The first term (Cherenkov effect) is in the 5% range based on simulations (the distribution of generated photons is characterized by Q1 = 690, Q2 = 725, and M = 708 in our bars). Fluctuations coming from the photomultiplier are at a level of 7% for a constant optical signal level. Fluctuation of signal due to transport in the bar thus dominates. This study did not take into account cross-talk contributions from the adjacent pixels (the bars were tested separately). We measured a higher level of fluctuations by 2 – 4% per bar when both bars per train were used. However, this result needs a verification.

6. Resolution of the trains

The aim of the ToF detector is the measurement of arrival time with a resolution below 20 ps. For the given configuration, we studied the timing performance with two bars per train only. For such studies we preprocessed the output signal by means of the CFD module, see Fig. 5. The timestamp of the leading edge was treated as the arrival time of a signal pulse. The arrival time of a signal pulse from the PMT was calculated with respect to the arrival time of the SiPM detector serving as a trigger (the first SiPM in the chain, see Fig. 5). The SiPM detectors were measured between each other to evaluate their time resolutions. The time resolution of the SiPM trigger was measured as 12 ps.

As an example, results of time measurements of the train 2 are plotted in Fig. 7. Note that the resolutions are calculated from the Gaussian fits. Here, the sigma values embody a

contribution from the trigger SiPM detector. The mean values are artificial and have no meaning. The arrival time of the train was calculated as the arithmetic average of the arrival times of each bar in the train. The distributions deviate from the Gaussian distribution at the tails. The origin of the tails is still not fully understood and it will be investigated in next test beam measurements.

The results of timing measurements are summarized in Table 2 for all trains. The contribution of the SiPM trigger was subtracted. We estimated the measurement error ± 2 ps based on results from 5 independent measurements. The measured resolutions vary with the position of the beam with respect to the train edge (see also Fig. 1 for the edge specification) due to the fact that the signal amplitude decreases with the distance from the edge (this effect was studied in [4]). At first sight, the B bars embody better timing resolutions compared to the A bars. This originates from the fact that the signal of the B bars is enriched by photons coming from the A bars. The infiltration takes place near the edges of the bars. According to simulations, the hit count of the B bars grows by 5% at the edge and by 40% at 5 mm from the edge. However, this optical cross-talk does not contribute to the signal correlation between bars because photons are generated independently and each photon contributes to a one channel (a PMT pixel) only. Assuming the case of four bars per train, all bars receive a contribution of photons generated in the foregoing bar except the first one. Thus the first bar suffers from a smaller hit count which could eventually result in a worse resolution based on the PMT response (timing resolution vs. number of photoelectrons, to be specific).
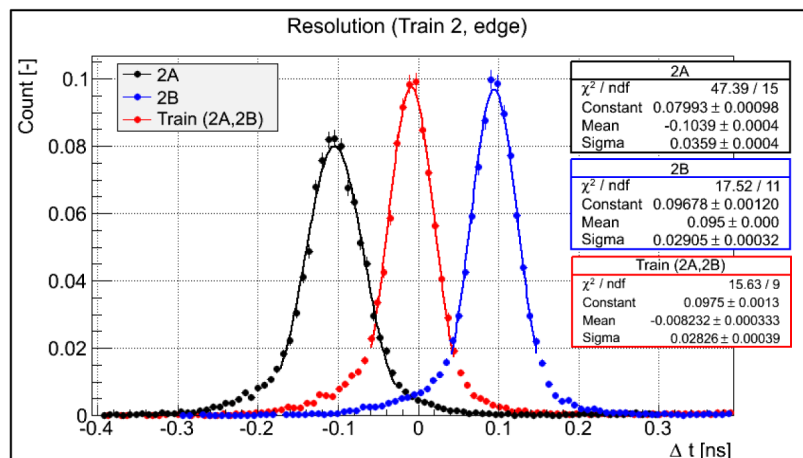

Fig. 7. Time resolution of the train 2 at the edge.

In Table 2, the resolution difference between the A bars and the B bars is emphasized at 5 mm from the edge (9 – 12 ps) compared to the edge position (5 – 8 ps). Only the 1A bar profited from its taper having a higher signal level, see Fig. 6(a), which partly compensated for the lack of signal. The resolution of the train arrival time is theoretically lower than the one of single bars by the factor $1/\sqrt{N}$, where N is the number of bars in the train, providing the output signals from the bars are mutually independent (uncorrelated) and the time resolutions of bars are similar. The latter condition is not apparently met in our case. We expect it to be more closely to the $1/\sqrt{N}$ rule for the full train scenario and a new PMT with better timing performance.

Correlations between bars generally worsen the time resolution of the whole train. A charge sharing between the PMT pixels causes a correlation between signal outputs at some level. Based on our raw signal analysis, we estimated the amplitude correlations to be approximately 10% between the A bars and the B bars caused by the charge sharing.

Table 2. Resolutions of the bars and the trains in picoseconds (estimated error ± 2 ps).

Train	Position	Bar A	Bar B	Whole train
1	edge	31	26	23
	5 mm from edge	40	31	28
2	edge	34	26	25
	5 mm from edge	42	31	33
3	edge	31	26	25
	5 mm from edge	41	31	34
4	edge	33	26	27
	5 mm from edge	42	29	33

Although we used only two bars per train, i.e. half of the design number of bars, the resolution values at the edge of the ToF detector are already close to the final specification of 10 – 20 ps. For next studies we plan to have a setup with four bars in trains and a PMT with suppressed charge sharing and a better timing performance.

7. Conclusion

We have presented the design, construction, and initial performance measurements of the ToF prototype for the AFP project. The selected geometry of the bars was determined and based on our previous simulation studies. The produced bars were tested at the CERN-SPS test-beam facility (120 GeV π + particles) in November 2014 and September 2015. Besides this, additional studies and measurements were performed to estimate the limits of the design, in particular the study of the elbow mirror reflection, and the transmission of suprasil and the glue in the deep UV region. Radiation hardness of these components are outside the scope of the paper and will be published separately.

The reflection on the mirror layer on the bar elbow introduces a loss of 10 – 12% and depends on the polarization state of the light as the Cherenkov light is strongly polarized. Our simulation studies showed that the p component of the incoming photons prevails over the s component (peak of s/p ratio at 0.34) in the frame of the bar design. Suprasil material has the transmission edge at 166 nm (for the thickness of 4 mm). For the wavelengths above this limit, the transmission reaches 91%. Concerning the glue, the main issue is a shift of the transmission edge up to 233 nm. This results in a signal loss of at least 20%.

Measurements in test beams at the SPS at CERN have proven the usefulness of the taper solution as described in [4] which increased the signal level by 30%. On the other hand, adding a taper results in a thinner radiator and therefore lower acceptance. Thus, in order to fully cover the required acceptance window, one needs either to omit the taper or to increase the number of trains. The latter option amounts to a higher pixelization.

The resolutions of the trains of bars were measured to be in the range from 20 to 33 ps and worsen with the increasing distance of the beam from the edge. In the presented setup, we focused on the overall timing performance of the ToF prototype with just two bars per train. A full train setup will be used in next test beam measurements, which will allow us to study more aspects of the ToF performance issues.